Stanford Exploration Project, Report 113, July 8, 2003, pages 177–210

Angle-domain common-image gathers for migration velocity analysis by wavefield-continuation imaging

Biondo Biondi and William Symes[1]

ABSTRACT

We analyze the kinematic properties of offset-domain Common Image Gathers (CIGs) and Angle-Domain CIGs (ADCIGs) computed by wavefield-continuation migration. Our results are valid regardless of whether the CIGs were obtained by using the correct migration velocity. They thus can be used as a theoretical basis for developing Migration Velocity Analysis (MVA) methods that exploit the velocity information contained in ADCIGs.

We demonstrate that in an ADCIG cube the image point lies on the normal to the apparent reflector dip, passing through the point where the source ray intersects the receiver ray. Starting from this geometric result, we derive an analytical expression for the expected movements of the image points in ADCIGs as functions of the traveltime perturbation caused by velocity errors. By applying this analytical result and assuming stationary raypaths, we then derive two expressions for the Residual Moveout (RMO) function in ADCIGs. We verify our theoretical results and test the accuracy of the proposed RMO functions by analyzing the migration results of a synthetic data set with a wide range of reflector dips.

Our kinematic analysis leads also to the development of a new method for computing ADCIGs when significant geological dips cause strong artifacts in the ADCIGs computed by conventional methods. The proposed method is based on the computation of offset-domain CIGs along the vertical-offset axis (VOCIGs) and on the "optimal" combination of these new CIGs with conventional CIGs. We demonstrate the need for and the advantages of the proposed method on a real data set acquired in the North Sea.

INTRODUCTION

With wavefield-continuation migration methods being used routinely for imaging project in complex areas, the ability to perform Migration Velocity Analysis (MVA) starting from the results of wavefield-continuation migration is becoming essential to advanced seismic imaging. As for Kirchhoff imaging, MVA for wavefield-continuation imaging is mostly based on the information provided by the analysis of Common Image Gather (CIGs). Most of the current MVA methods start from Angle-Domain CIGs (ADCIGs) (Biondi and Sava, 1999; Clapp

[1]**email:** biondo@sep.stanford.edu

and Biondi, 2000; Mosher et al., 2001; Liu et al., 2001), though the use of more conventional surface-offset-domain CIGs is also being evaluated (Stork et al., 2002).

Both kinematic and amplitude properties (de Bruin et al., 1990; Wapenaar et al., 1999; Sava et al., 2001; de Hoop et al., 2002) have been analyzed in the literature for ADCIGs obtained when the migration velocity is accurate. On the contrary, the properties of the ADCIGs obtained when the migration velocity is inaccurate have been only qualitatively discussed in the literature. This lack of quantitative understanding may lead to errors when performing MVA from ADCIGs. In this paper, we analyze the kinematic properties of ADCIGs under general conditions (accurate or inaccurate velocity). If the migration velocity is inaccurate, our analysis requires only a smooth migration velocity function in the neighborhood of the imaging point. We discuss this condition more extensively in the first section. The application of the insights provided by our analysis may substantially improve the results of the following three procedures: a) measurement of velocity errors from ADCIGs by residual moveout (RMO) analysis, b) inversion of RMO measurements into velocity updates, and c) computation of ADCIGs in the presence of complex geologic structure.

Our analysis demonstrates that in an ADCIG cube the image point lies on the normal to the apparent reflector dip passing through the point where the source ray intersects the receiver ray. We exploit this result to define an analytical expression for the expected movements of the image points in ADCIGs as a function of the traveltime perturbation caused by velocity errors. This leads us to the definition of two alternative residual moveout functions that can be applied when measuring velocity errors from migrated images. We test the accuracy of these alternatives and discuss their relative advantages and disadvantages. Furthermore, the availability of a quantitative expression for the expected movements of the image points is crucial when inverting those movements into velocity corrections by either simple vertical updating or sophisticated tomographic methods. Therefore, our results ought to be incorporated in velocity updating methods.

Our theoretical result also implies that ADCIGs are immune, at least at first order, from the distortions caused by *image-point dispersal*. Image-point dispersal occurs when migration velocity errors cause events from the same segment of a dipping reflector to be imaged at different locations (Etgen, 1990). This inconsistency creates substantial problems when using dipping reflections for velocity updating; its absence makes ADCIGs even more attractive for MVA.

The computation of ADCIGs is based on a decomposition (usually performed by slant-stacks) of the wavefield either before imaging (Mosher et al., 1997; Prucha et al., 1999; Xie and Wu, 2002), or after imaging (Sava and Fomel, 2002; Rickett and Sava, 2002; Biondi and Shan, 2002). In either case, the slant stack transformation is usually applied along the horizontal subsurface-offset axis. However, when the geologic dips are steep, this "conventional" way of computing CIGs does not produce useful gathers, even if it is kinematically valid for geologic dips milder than 90 degrees. As the geologic dips increase, the horizontal-offset CIGs (HOCIGs) degenerate, and their focusing around zero offset blurs. This limitation of HOCIGs can be sidestepped by computing offset-domain CIGs along the vertical subsurface-offset axis (VOCIGs) (Biondi and Shan, 2002). Although neither set of offset-domain gathers (HOCIG

or VOCIG) provides useful information for the whole range of geologic dips, an appropriate combination of the two sets does. Our analysis of the kinematic properties of ADCIGs suggests a simple and effective method for combining a HOCIG cube with a VOCIG cube to create an ADCIG cube that is immune to artifacts in the presence of arbitrary geologic dips.

The plan of attack for covering the broad, but interrelated, set of issues that are relevant to the use of ADCIGs for MVA is the following. We start by briefly reviewing the methodology for computing offset-domain and angle-domain CIGs by wavefield-continuation migration. The second section analyzes the kinematic properties of CIGs and ADCIGs, and contains the main theoretical development of the paper. The third section exploits the theoretical results to define a robust algorithm to compute ADCIGs in the presence of geological structure and illustrates its advantages with a real-data example. The fourth section verifies the theoretical analysis by using it to predict reflector movements in the migrated images of a synthetic data set. Finally, the fifth section derives two expressions for the RMO function to be applied for measuring velocity errors from migrated images.

COMPUTATION OF COMMON IMAGE GATHERS BY WAVEFIELD CONTINUATION

In this section we briefly revisit the method for computing Common Image Gathers (CIG) by wavefield-continuation migration. The following development assumes that both the source wavefield and the receiver wavefield have been numerically propagated into the subsurface. The analytical expressions represent wavefields in the time domain, and thus they appear to implicitly assume that the wavefields have been propagated in the time domain. However, all the considerations and results that follow are independent of the specific numerical method that was used for propagating the wavefields. They are obviously valid for reverse-time migration when the wavefields are propagated in the time domain (Whitmore, 1983; Baysal et al., 1983; Etgen, 1986; Biondi and Shan, 2002). They are also valid when the wavefields are propagated by downward continuation in the frequency domain, if there are no overturned events. The results presented in this paper are valid even when source-receiver migration is used instead of shot-profile migration, if the conditions are satisfied for these two apparently dissimilar methods to be equivalent (Biondi, 2003).

The conventional imaging condition for shot-profile migration is based on the crosscorrelation in time of the source wavefield (S) with the receiver wavefield (R). The equivalent of the stacked image is the average over sources (s) of the zero lag of this crosscorrelation; that is:

$$I(z,x) = \sum_s \sum_t S_s(t,z,x)\, R_s(t,z,x), \tag{1}$$

where z and x are respectively depth and the horizontal axes, and t is time. The result of this imaging condition is equivalent to stacking over offsets with Kirchhoff migration.

The imaging condition expressed in equation (1) has the substantial disadvantage of not providing prestack information that can be used for either velocity updates or amplitude analysis. Equation (1) can be generalized (de Bruin et al., 1990; Rickett and Sava, 2002; Biondi

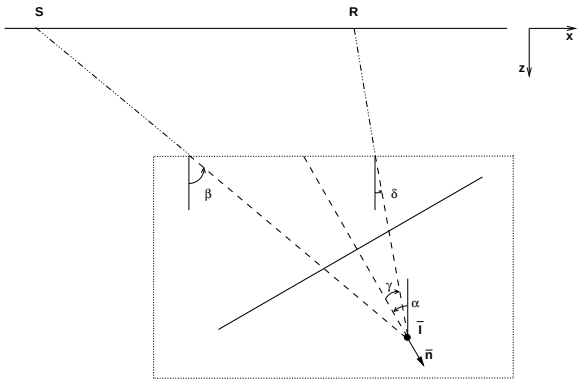

Figure 1: Geometry of an ADCIG for a single event migrated with the wrong (low in this case) velocity. The propagation direction of the source ray forms the angle β with the vertical, and the propagation direction of the receiver ray forms the angle δ with the vertical; γ is the apparent aperture angle, and α is the apparent reflector dip. The source ray and the receiver ray cross at $\bar{I}$. Notice that in this figure β, δ and α are positive, but γ is negative. biondo1-cig-simple-v2 [NR]

and Shan, 2002) by crosscorrelating the wavefields shifted horizontally with respect to each other. The prestack image becomes a function of the horizontal relative shift, which has the physical meaning of a *subsurface half offset* (x_h). It can be computed as

$$I(z,x,x_h) = \sum_s \sum_t S_s(t,z,x-x_h)\, R_s(t,z,x+x_h). \tag{2}$$

A section of the image cube taken at constant horizontal location x is a Horizontal Offset Common Image Gather, or HOCIG. The whole image cube can be seen as a collection of HOCIGs.

Sava and Fomel (2002) presented a simple method for transforming HOCIGs into ADCIGs by a slant stack transformation applied independently to each HOCIG (Schultz and Claerbout, 1978):

$$I_{\gamma_x}(z,x,\gamma) = \text{SlantStack}[I(z,x,x_h)]; \tag{3}$$

where γ is the aperture angle of the reflection, as shown in Figure 1. This transformation from HOCIG to ADCIG is based on the following relationship between the aperture angle and the slope, $\partial z/\partial x_h$, measured in image space:

$$\left.\frac{\partial z}{\partial x_h}\right|_{t,x} = \tan\gamma = -\frac{k_{x_h}}{k_z}; \tag{4}$$

where k_{x_h} and k_z are respectively the half-offset wavenumber and the vertical wavenumber. The relationship between $\tan\gamma$ and the wavenumbers also suggests that the transformation to ADCIGs can be accomplished in the Fourier domain by a simple radial-trace transform (Sava and Fomel, 2002).

Sava and Fomel (2002) demonstrated the validity of equation (4) based only on Snell's law and on the geometric relationships between the propagation directions of the source ray (determined by β in Figure 1) and receiver ray (determined by δ in Figure 1). Its validity

is thus independent of the focusing of the reflected energy at zero offset; that is, it is valid regardless of whether the image point coincides with the intersection of the two rays (marked as $\bar{I}$ in Figure 1). In other words, it is independent of whether the correct migration velocity is used. The only assumption about the migration velocity is that the velocity at the imaging depth is locally the same along the source ray and the receiver ray. This condition is obviously fulfilled when the reflected energy focuses at zero offset, but it is, at least approximately, fulfilled in most practical situations of interest. In most practical cases we can assume that the migration velocity function is smooth in a neighborhood of the imaging point, and thus that the velocity at the end point of the source ray is approximately the same as the velocity at the end point of the receiver ray. The only exception of practical importance is when the reflection is caused by a high-contrast interface, such as a salt-sediment interface. In these cases, our results must be applied with particular care. When the migration velocity is correct, α and γ are respectively the true reflector dip and the true aperture angle; otherwise they are the *apparent* dip and the apparent aperture angle. In Figure 1, the box around the imaging point signifies the local nature of the geometric relationships relevant to our discussion; it emphasizes that these relationships depend only on the local velocity function.

When the velocity is correct, the image point obviously coincides with the crossing point of the two rays $\bar{I}$. However, the position of the image point when the velocity is not correct has been left undefined by previous analyses (Prucha et al., 1999; Sava and Fomel, 2002). In this paper, we demonstrate the important result that in an ADCIGs, when the migration velocity is incorrect, the image point lies along the direction normal to the apparent geological dip. We identify this normal direction with the unit vector **n** that we define as oriented in the direction of increasing traveltimes for the rays (see Figure 1).

Notice that the geometric arguments presented in this paper are based on the assumption that the source and receiver rays cross, even when the data were migrated with the wrong velocity. This assumption is valid in 2-D except in degenerate cases of marginal practical interest (e.g. diverging rays). In 3-D, this assumption is more easily violated, because the two rays are not always coplanar. This discrepancy between 2-D and 3-D geometries makes the generalization to 3-D of the results presented in this paper less than trivial. Therefore, we consider the 3-D generalization beyond the scope of this paper.

As will be discussed in the following and exemplified by the real-data example in Figure 6a, the HOCIGs, and consequently the ADCIGs computed from the HOCIGs (Figure 7a), have problems when the reflectors are steeply dipping. At the limit, the HOCIGs become useless when imaging almost vertical reflectors using either overturned events or prismatic reflections. To create useful ADCIGs in these situations we introduce a new kind of CIGs (Biondi and Shan, 2002). This new kind of CIG is computed by introducing a *vertical half offset* (z_h) into equation (1) to obtain:

$$I(z,x,z_h) = \sum_s \sum_t S_s(t, z-z_h, x)\, R_s(t, z+z_h, x). \tag{5}$$

A section of the image cube computed by equation (5) taken at constant depth z is a Vertical Offset Common Image Gathers, or VOCIG.

As for the HOCIGs, the VOCIGs can be transformed into an ADCIG by applying a slant

stack transformation to each individual VOCIG; that is:

$$I_{\gamma_z}(z,x,\gamma) = \text{SlantStack}[I(z,x,z_h)]. \tag{6}$$

This transformation is based on the following relationship between the aperture angle and the slope $\partial x/\partial z_h$ measured in image space:

$$-\left.\frac{\partial x}{\partial z_h}\right|_{t,z} = \tan\gamma = \frac{k_{z_h}}{k_x}. \tag{7}$$

Equation (7) is analogous to equation (4), and its validity can be trivially demonstrated from equation (4) by a simple axes rotation. However, notice the sign differences between equation (7) and equation (4) caused by the conventions defined in Figure 1.

Notice that our notation distinguishes the result of the two transformations to ADCIG $\left(I_{\gamma_x}$ and $I_{\gamma_z}\right)$, because they are different objects even though they are images defined in the same domain (z,x,γ). One of the main results of this paper is the definition of the relationship between I_{γ_x} and I_{γ_z}, and the derivation of a robust algorithm to "optimally" merge the two sets of ADCIGs. To achieve this goal we will first analyze the kinematic properties of HOCIGs and VOCIGs.

KINEMATIC PROPERTIES OF COMMON IMAGE GATHERS

In this section we analyze the kinematic properties of CIGs, with particular emphasis on the case when velocity errors prevent the image from focusing at zero offset, causing the reflected energy to be imaged over a range of offsets. We will start by analyzing the kinematics of offset-domain CIGs.

To analyze the kinematic properties of HOCIGs and VOCIGs, it is useful to observe that they are just particular cases of offset-domain gathers. In general, the offset can be oriented along any arbitrary direction. In particular, the offset direction aligned with the apparent geological dip of the imaged event has unique properties. We will refer to this offset as the *geological-dip offset*, and the corresponding CIGs as Geological Offset CIGs, or GOCIGs.

Figure 2 illustrates the geometry of the different kinds of offset-domain CIGs for a single event. In this sketch, the migration velocity is assumed to be lower than the true velocity, and thus the reflections are imaged too shallow and above the point where the source ray crosses the receiver ray ($\bar{I}$). The line passing through $\bar{I}$, and bisecting the angle formed by the source and receiver ray, is oriented at an angle α with respect to the vertical direction. The angle α is the apparent geological dip of the event after imaging. Half of the angle formed between the source and receiver ray is the apparent aperture angle γ.

When HOCIGs are computed, the end point of the source ray (S_{x_h}) and the end point of the receiver ray (R_{x_h}) are at the same depth. The imaging point I_{x_h} is midway between S_{x_h} and R_{x_h}, and the imaging half offset is $x_h = R_{x_h} - I_{x_h}$. Similarly, when VOCIGs are computed, the end point of the source ray (S_{z_h}) and the end point of the receiver ray (R_{z_h}) are at the same horizontal location. The imaging point I_{z_h} is midway between S_{z_h} and R_{z_h}, and the imaging

half offset is $z_h = R_{z_h} - I_{z_h}$. When the offset direction is oriented along the apparent geological dip α (what we called the geological-dip offset direction), the end point of the source ray is S_0 and the end point of the receiver ray is R_0. The imaging point I_0 is midway between S_0 and R_0, and the imaging half offset is $\mathbf{h}_0 = R_0 - I_0$. Notice that the geological-dip half offset $\mathbf{h}_0$ is a vector, because it can be oriented arbitrarily with respect to the coordinate axes.

Figure 2 shows that both I_{x_h} and I_{z_h} lie on the line passing through S_0, I_0 and R_0. This is an important property of the offset-domain CIGs and is based on a crucial constraint imposed on our geometric construction; that is, the traveltime along the source ray summed with the traveltime along the receiver ray is the same for all the offset directions, and is equal to the recording time of the event. The independence of the total traveltimes from the offset directions is a direct consequence of taking the zero lag of the crosscorrelation in the imaging conditions of equation (2) and (5). This constraint, together with the assumption of locally constant velocity that we discussed above, directly leads to the following equalities:

$$\left|S_{x_h} - S_0\right| = \left|R_{x_h} - R_0\right|, \quad \text{and} \quad \left|S_{z_h} - S_0\right| = \left|R_{z_h} - R_0\right|, \tag{8}$$

which in turn are at the basis of the collinearity of I_0, I_{x_h} and I_{z_h}.

The offsets along the different directions are linked by the following simple relationship, which can be readily derived by trigonometry applied to Figure 2:

$$x_h = \frac{\widetilde{h_0}}{\cos\alpha}, \tag{9}$$

$$z_h = -\frac{\widetilde{h_0}}{\sin\alpha}, \tag{10}$$

where $\widetilde{h_0} = \mathbf{n} \times \mathbf{h}_0$. Notice that the definition of $\widetilde{h_0}$ is such that its sign depends on whether I_0 is before or beyond $\bar{I}$, and that for flat events ($\alpha = 0$) we have $\widetilde{h_0} = x_h$.

Although I_{x_h} and I_{z_h} are both collinear with I_0, they are shifted with respect to each other and with respect to I_0. The shifts of the imaging points I_{x_h} and I_{z_h} with respect to I_0 can be easily expressed in terms of the offset $\mathbf{h}_0$ and the angles α and γ as follows:

$$\Delta\mathbf{I}_{x_h} = \left(I_{x_h} - I_0\right) = \mathbf{h}_0 \tan\gamma \tan\alpha, \tag{11}$$

$$\Delta\mathbf{I}_{z_h} = \left(I_{z_h} - I_0\right) = -\mathbf{h}_0 \frac{\tan\gamma}{\tan\alpha}. \tag{12}$$

The shift between I_{x_h} and I_{z_h} prevents us from constructively averaging HOCIGs with VOCIGs to create a single set of offset-domain CIGs.

Notice the dependence of $\Delta\mathbf{I}_{x_h}$ and $\Delta\mathbf{I}_{z_h}$ on the aperture angle γ. This dependence causes events with different aperture angles to be imaged at different locations, even if they originated at the same reflecting point in the subsurface. This phenomenon is related to the well known *reflector-point dispersal* in common midpoint gathers. In this context, this dispersal is a consequence of using a wrong imaging velocity, and we will refer to it as *image-point dispersal*. We will now discuss how the transformation to ADCIGs overcomes the problems related to the image-point shift and thus removes, at least at first order, the image-point dispersal.

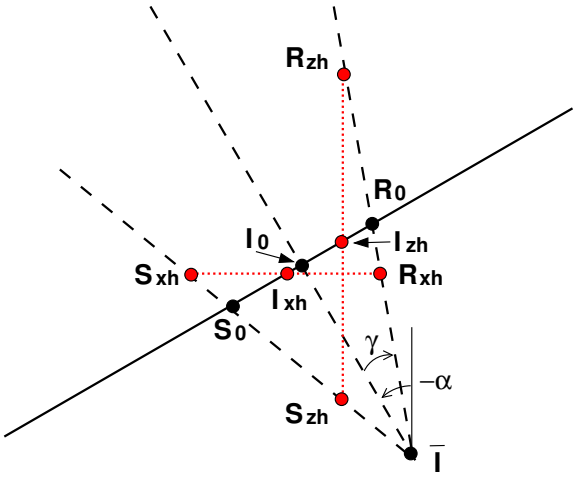

Figure 2: Geometry of the three different kinds of offset-domain (horizontal, vertical and geological-dip) CIG for a single event migrated with the wrong velocity. I_{x_h} is the horizontal-offset image point, I_{z_h} is the vertical-offset image point, and I_0 is the geological-dip offset image point. biondo1-cig-gen-v6 [NR]

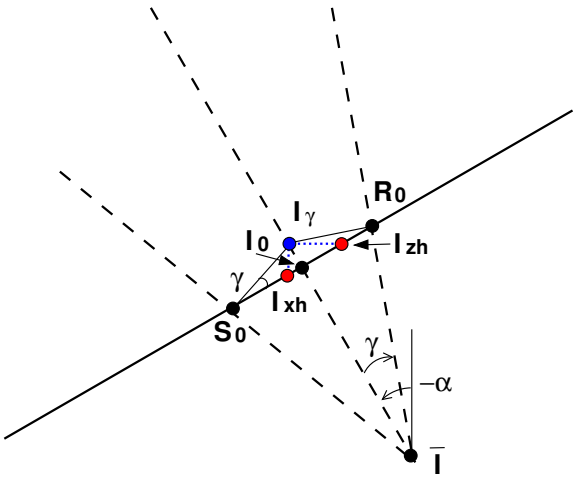

Figure 3: Geometry of an angle-domain CIG for a single event migrated with the wrong velocity. The transformation to the angle domain shifts all the offset-domain image points (I_{x_h}, I_{z_h},I_0) to the same angle-domain image point I_γ. biondo1-cig-image-dip-v2 [NR]

Kinematic properties of ADCIGs

The transformation to the angle domain, as defined by equations (3–4) for HOCIGs and equations (6–7) for VOCIGs, acts on each offset-domain CIG independently. Therefore, when the reflected energy does not focus at zero offset, the transformation to the angle domain shifts the image point along the direction orthogonal to the offset. The horizontal-offset image point (I_{x_h}) shifts vertically, and the vertical-offset image point (I_{z_h}) shifts horizontally. We will demonstrate the two following important properties of this *normal shift*:

I) The normal shift corrects for the effects of the offset direction on the location of the image point; that is, the transformation to the angle domain shifts the image points from different locations in the offset domain (I_{x_h}, I_{z_h} and I_0) to the same location in the angle domain (I_γ).

II) The image location in the angle domain (I_γ) lies on the normal to the apparent geological dip passing through the crossing point of the source and receiver rays ($\bar{I}$). I_γ is located at the crossing point of the lines passing through S_0 and R_0 and orthogonal to the source ray and receiver ray, respectively. The shift along the normal to the reflector, caused by the transformation to angle domain, is thus equal to:

$$\Delta\mathbf{n}_\gamma = \left(I_\gamma - I_0\right) = \widetilde{h}_0 \tan\gamma\,\mathbf{n} = \tan^2\gamma\ \Delta\mathbf{n}_{h_0}, \tag{13}$$

where $\Delta\mathbf{n}_{h_0} = \left(\widetilde{h}_0/\tan\gamma\right)\mathbf{n}$ is the normal shift in the geological-dip domain. The total normal shift caused by incomplete focusing at zero offset is thus equal to:

$$\Delta\mathbf{n}_{\text{tot}} = \left(I_\gamma - \bar{I}\right) = \Delta\mathbf{n}_{h_0} + \Delta\mathbf{n}_\gamma = \Delta\mathbf{n}_{h_0}\left(1+\tan^2\gamma\right) = \frac{\Delta\mathbf{n}_{h_0}}{\cos^2\gamma}. \tag{14}$$

Figure 3 illustrates Properties I and II. These properties are far from obvious and their demonstration constitutes one of the main results of this paper. They also have several important consequences; the three results most relevant to migration velocity analysis are:

1. ADCIGs obtained from HOCIGs and VOCIGs can be constructively averaged, in contrast to the original HOCIGs and VOCIGs. We will exploit this property to introduce a robust algorithm for creating a single set of ADCIGs that is insensitive to geological dips, and thus is ready to be analyzed for velocity information.

2. The reflector-point dispersal that negatively affects offset-domain CIGs is corrected in the ADCIGs, at least at first order. If we assume the raypaths to be stationary, for a given reflecting segment the image points for all aperture angles γ share the same apparent dip, and thus they are all aligned along the normal to the apparent reflector dip.

3. From equation (14), invoking Fermat's principle and applying simple trigonometry, we can also easily derive a relationship between the total normal shift $\Delta\mathbf{n}_{\text{tot}}$ and the total traveltime perturbation caused by velocity errors as follows:

$$\Delta\mathbf{n}_{\text{tot}} = -\frac{\Delta t}{2S\cos\gamma}\mathbf{n}, \tag{15}$$

where S is the background slowness around the image point and Δt is defined as the difference between the perturbed traveltime and the background traveltime. We will exploit this relationship to introduce a simple and accurate expression for measuring residual moveouts from ADCIGs.

Demonstration of kinematic properties of ADCIGs

Properties I and II can be demonstrated in several ways. In this paper, we will follow an indirect path that might seem circuitous but will allow us to gather further insights on the properties of ADCIGs.

We first demonstrate Property I by showing that the radial-trace transformations represented by equation (4), and analogously equation (7), are equivalent to a chain of two transformations. The first one is the transformation of the HOCIGs (or VOCIGs) to GOCIGs by a dip-dependent stretching of the offset axis; that is:

$$\widetilde{h_0} = x_h \cos\alpha, \quad \text{or} \quad \widetilde{h_0} = -z_h \sin\alpha; \tag{16}$$

or in the wavenumber domain,

$$k_{h_0} = \frac{k_{x_h}}{\cos\alpha}, \quad \text{or} \quad k_{h_0} = -\frac{k_{z_h}}{\sin\alpha}; \tag{17}$$

where k_{h_0} is the wavenumber associated with $\widetilde{h_0}$, and k_{x_h} and k_{z_h} are the wavenumbers associated with x_h and z_h.

The second is the transformation of HOCIGs to the angle domain according to the relation

$$\tan\gamma = -\frac{k_{h_0}}{k_n}, \tag{18}$$

where k_n is the wavenumber associated with the direction normal to the reflector. This direction is identified by the line passing through $\bar{I}$ and I_γ in Figures 2 and 3.

The transformation of HOCIGs to GOCIGs by equations (16) and (17) follows directly from equations (9) and (10). Because the transformation is a dip-dependent stretching of the offset axis, it shifts energy in the (z,x) plane. Appendix A demonstrates that the amount of shift in the (z,x) plane exactly corrects for the image-point shift characterized by equations (11) and (12).

Appendix B demonstrates the geometrical property that for energy dipping at an angle α in the the (z,x) plane, the wavenumber k_n along the normal to the dip is linked to the wavenumbers along (z,x) by the following relationships:

$$k_n = \frac{k_z}{\cos\alpha} = \frac{k_x}{\sin\alpha}. \tag{19}$$

Substituting equations (17) and (19) into equation (18), we obtain equations (4) and (7). The graphical interpretation of this analytical result is immediate. In Figure 3, the transformation

to GOCIG [equations (17)] moves the imaging point I_{x_h} (or I_{z_h}) to I_0, and the transformation to the angle domain [equation (18)] moves I_0 to I_γ. This sequence of two shifts is equivalent to the direct shift from I_{x_h} (or I_{z_h}) to I_γ caused by the transformation to the angle domain applied to a HOCIG (or VOCIG).

We just demonstrated that the transformation to ADCIG is independent from which type of offset-domain CIGs we started from (HOCIG, VOCIG, or GOCIG). Consequently, the imaging point I_γ must be common to all kinds of ADCIGs. Furthermore, the image point must lie along each of the normals to the offset directions passing through the respective image points. In particular, it must lie along the normal to the apparent geological dip, and at the crossing point of the the vertical line passing through I_{x_h} and the horizontal line passing through I_{z_h}.

Given these constraints, the validity of Property II [equations (13) and (14)] can be easily verified by trigonometry, assuming that the image-point shifts are given by the expressions in equations (9) and (10). However, we will now demonstrate Property II in an alternative way; that is, by analyzing a GOCIG computed from an event with no apparent geological dip ($\alpha = 0$). This analysis provides intuitive understanding of the relation between offset-domain and angle domain CIGs when the migration velocity is incorrect. Furthermore, the analysis of a GOCIG with flat dip is representative of all the GOCIGs, as a rotation of Figure 3 suggests.

Figure 4 shows the geometry of a GOCIG with flat apparent dip. In this particular case, the imaging condition for ADCIGs has a direct "physical" explanation. The source and receiver rays can be associated with the corresponding planar wavefronts propagating in the same direction (and thus tilted by an angle γ with respect to the horizontal). The crosscorrelation of the plane waves creates the angle-domain image point I_γ where the plane waves intersect. I_γ is shifted vertically by $\widetilde{h}_0 \tan\gamma$ with respect to the offset-domain imaging point I_0. In this case, there is also a direct connection between the computation of ADCIGs in the image space and the computation of ADCIGs in the data space by plane-wave decomposition of the full prestack wavefield obtained by recursive survey sinking (Prucha et al., 1999).

The interpretation of ADCIGs in the "physical" space (Figure 4) can also be easily connected to the effects of applying slant stacks in the image space (Figure 5). Migration of a prestack flat event with too low a migration velocity generates an incompletely focused hyperbola in the image space, as sketched in Figure 5. According to equation (4), the tangent to the hyperbola at offset $\widetilde{h}_0 = x_h$ has the slope $\partial z/\partial x_h = -\tan\gamma$. This tangent intersects the vertical axis at a point shifted by $\Delta\mathbf{n}_\gamma = \widetilde{h}_0 \tan\gamma\,\mathbf{n}$ from I_0.

In the more general case of dipping reflectors (i.e. with $\alpha \neq 0$), when $x_h = \widetilde{h}_0/\cos\alpha$, the shift along the vertical is $x_h \tan\gamma\,\mathbf{n} = \left(\widetilde{h}_0 \tan\gamma/\cos\alpha\right)\mathbf{n}$. This result is consistent with the geometric construction represented in Figure 3.

ROBUST COMPUTATION OF ADCIGS IN PRESENCE OF GEOLOGICAL STRUCTURE

Our first application of the CIG kinematic properties analyzed in the previous section is the definition of a robust method to compute high-quality ADCIGs for all events, including steeply

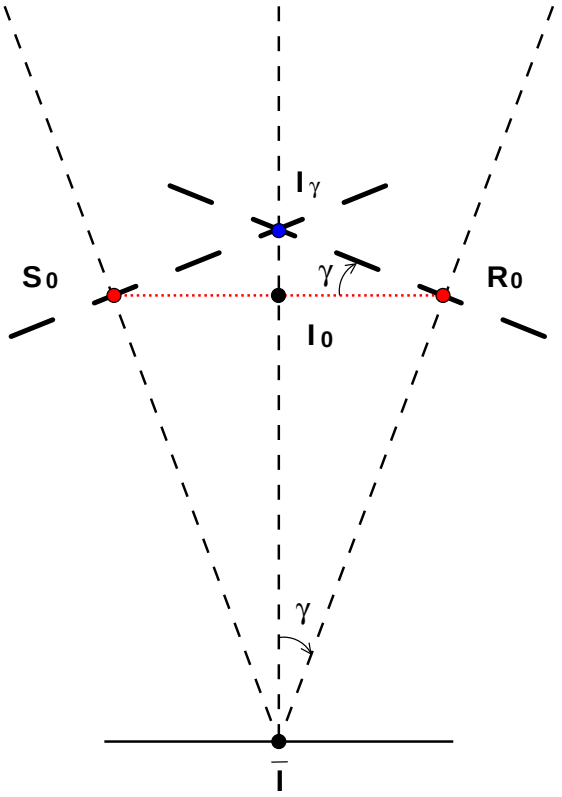

Figure 4: Geometry of a GOCIG with flat apparent dip. In this case, the source and receiver rays can be associated with the corresponding planar wavefronts propagating in the same direction. The crosscorrelation of the plane waves creates the angle-domain image point I_γ where the plane waves intersect. biondo1-cig-flat-v1 [NR]

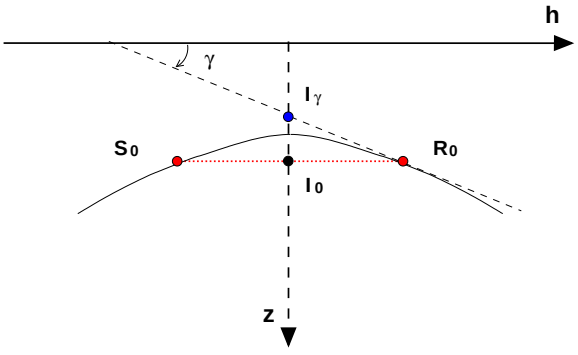

Figure 5: Graphical analysis of the application of slant stacks to a GOCIG when an event with flat apparent dip is migrated with a low velocity. The event is an incompletely focused hyperbola in the image space. The tangent of this hyperbola at $\mathbf{h}_0$ crosses the vertical axis at I_γ. biondo1-cig-image-v1 [NR]

dipping and overturned reflections. In presence of complex geological structure, the computation of neither the conventional HOCIGS nor the new VOCIGs is sufficient to provide complete velocity information, because the image is stretched along both the subsurface-offset axes.

According to equation (9), as the geological dip increases the horizontal-offset axis is stretched. At the limit, when α is equal to 90 degrees, the relation between the horizontal-offset and the geological-dip offset becomes singular. Similarly, VOCIGs have problems when the geological dip is close to flat ($\alpha = 0$ degrees) and equation (10) becomes singular. This dip-dependent offset-stretching of the offset-domain CIGs causes artifacts in the corresponding ADCIGs.

The fact that relationships (9) and (10) diverge only for isolated dips (0, 90, 180, and 270 degrees) may falsely suggest that problems are limited to rare cases. However, in practice there are two factors that contribute to make the computation of ADCIGs in presence of geological dips prone to artifacts:

- To limit the computational cost, we would like to compute the offset-domain gathers over a range of offsets as narrow as possible. This is particularly true for shot-profile migrations, where the computation of the imaging conditions by equation (2) can add substantially to the computational cost when it is carried over a wide range of subsurface offsets.

- The attractive properties of the ADCIGs that we demonstrated above, including the elimination of the image-point dispersal, depend on the assumption of locally constant velocity. In particular, velocity is assumed to be constant along the ray segments $\overline{S_{x_h} S_0}$, $\overline{R_{x_h} R_0}$, $\overline{S_{z_h} S_0}$, and $\overline{R_{z_h} R_0}$ drawn in Figure 2. The longer those segments are, the more likely it is that the constant velocity assumption will be violated sufficiently to cause substantial errors.

These considerations suggest that, in presence of complex structures, high-quality ADCIGs ought to be computed using the information present in both HOCIGs and VOCIGs. There are two alternative strategies for obtaining a single set of ADCIGs from the information present in HOCIGs and VOCIGs. The first method merges HOCIGs with VOCIGs after they have been transformed to GOCIGs by the application of the offset stretching expressed in equation (16). The merged GOCIGs are then transformed to ADCIGs by applying the radial-trace transformation expressed in equation (18). The second method merges HOCIGs with VOCIGs directly in the angle domain, after both have been transformed to ADCIGs by the radial-trace transforms expressed in equations (4) and (7).

The two methods are equivalent if the offset range is infinitely wide, but they may have different artifacts when the offset range is limited. Since the first method merges the images in the offset domain, it can take into account the offset-range limitation more directly, and thus it has the potential to produce more accurate ADCIGs. However, the second method is more direct and simpler to implement. In both methods, an effective, though approximate, way for taking into account the limited offset ranges is to weight the CIGs as a function of the apparent

dips α in the image. A simple weighting scheme is:

$$\begin{aligned} w_{x_h} &= \cos^2\alpha, \\ w_{z_h} &= \sin^2\alpha, \end{aligned} \tag{20}$$

where the weights w_{x_h} and w_{z_h} are respectively for the CIGs computed from the HOCIGs and the VOCIGs. These weights have the attractive property that their sum is equal to one for any α. We used this weighting scheme for all the results shown in this paper.

ADCIGs in the presence of geological structure: a North Sea example

The following marine-data example demonstrates that the application of the robust method for computing ADCIGs presented in this section substantially improves the quality of ADCIGs in the presence of geological structure. Our examples show migration results of a 2-D line extracted from a 3-D data set acquired in the North Sea over a salt body with a vertical edge. The data were imaged using a shot-profile reverse time migration, because the reflections from the salt edge had overturned paths.

As predicted by our theory, in the presence of a wide range of reflector dips (e.g. flat sediments and salt edges), both the HOCIGS and the VOCIGs are affected by artifacts. Figure 6 illustrates this problem. It displays orthogonal sections cut through the HOCIG cube (Figure 6a), and through the VOCIG cube (Figure 6b). The front faces show the images at zero offset and are the same in the two cubes. The side face of Figure 6a shows the HOCIGs taken at the horizontal location corresponding to the vertical salt edge. We immediately notice that, at the depth interval corresponding to the salt edge, the image is smeared along the offset axis, which is consistent with the horizontal-offset stretch described by equation (9). On the contrary, the image of the salt edge is well focused in the VOCIG displayed in the top face of Figure 6b, which is consistent with the vertical-offset stretch described by equation (10). However, the flattish reflectors are unfocused in the VOCIG cube, whereas they are well focused in the HOCIG cube. The stretching of the offset axes causes useful information to be lost when significant energy is pushed outside the range of offsets actually computed. In this example, the salt edge reflection is clearly truncated in the HOCIG cube displayed in Figure 6a, notwithstanding that the image was computed for a fairly wide offset-range (800 meters, starting at -375 meters and ending at 425 meters).

The ADCIGs computed from either the HOCIGs or the VOCIGS have similar problems with artifacts caused by the wide range of reflectors dips. Figure 7 shows the ADCIG computed from the offset-domain CIGs shown in Figure 6. The salt edge is smeared in the ADCIG computed from HOCIG (side face of Figure 7a), whereas it is fairly well focused in the ADCIG computed from VOCIG (top face of Figure 7b). Conversely, the flattish reflectors are well focused in the ADCIG computed from HOCIG, whereas they are smeared in the ADCIG computed from VOCIG.

The artifacts mostly disappear when the ADCIG cubes shown in Figure 7 are merged according to the simple scheme discussed above, which uses the weights defined in equations (20). Figure 8 shows the ADCIG cube resulting from the merge. The moveouts for the

salt edge and the sediment reflections are now clearly visible in the merged ADCIG cube and could be analyzed for extracting velocity information. To confirm these conclusions we migrated the same data after scaling the slowness function with a constant factor equal to 1.04. Figure 9 shows the ADCIG cubes computed from the HOCIG cube (Figure 9a), and from the VOCIG cube (Figure 9b). When comparing Figure 7 with Figure 9, we notice the 175-meter horizontal shift of the salt edge reflection toward the left, caused by the decrease in migration velocity. However, the artifacts related to the salt edge reflection are similar in the two figures, and they similarly obscure the moveout information. On the contrary, the moveout information is ready to be analyzed in the cube displayed in Figure 10, which shows the ADCIG cube resulting from the merge of the ADCIG cubes shown in Figure 9. In particular, both the flattish event above the salt edge (at about 1,000 meters depth) and the salt edge itself show a typical upward smile in the angle-domain gathers, indicating that the migration velocity was too slow.

ILLUSTRATION OF CIGS KINEMATIC PROPERTIES WITH A SYNTHETIC DATA SET

To verify the results of our geometric analysis of the kinematic properties of CIGs, we modeled and migrated a synthetic data set with a wide range of dips. The reflector has spherical shape with radius of 500 m. The center is at 1,000 meters depth and 3,560 meters horizontal coordinate. The velocity is constant and equal to 2,000 m/s. The data were recorded in 630 shot records. The first shot was located at a surface coordinate of -2,000 meters, and the shots were spaced 10 meters apart. The receiver array was configured with an asymmetric split-spread geometry. The minimum negative offset was constant and equal to -620 meters. The maximum offset was 4,400 meters for all the shots, with the exception of the first 100 shots (from -2,000 meters to -1,000 meters), where the maximum offset was 5,680 meters to record all the useful reflections. To avoid boundary artifacts at the top of the model, both sources and receivers were buried 250 meters deep. Some of the reflections from the top of the sphere were muted out before migration to avoid migration artifacts caused by spurious correlations with the first arrival of the source wavefield. The whole data set was migrated twice: first using the correct velocity (2,000 m/s), and second after scaling the slowness function by a constant factor $\rho = 1.04$ (corresponding to a velocity of 1,923 m/s). The ADCIGs shown in this section and the following section were computed by merging the ADCIGs computed from both the HOCIGs and VOCIGs according to the robust algorithm presented in the previous section.

Figure 11a shows the zero-offset section (stack) of the migrated cubes with the correct velocity and Figure 11b shows the zero-offset section obtained with the low velocity. Notice that, despite the large distance between the first shot and the left edge of the sphere (about 5,000 meters), normal incidence reflections illuminate the target only up to about 70 degrees. As we will see in the angle-domain CIGs, the aperture angle coverage shrinks dramatically with increasing reflector dip. On the other hand, real data cases are likely to have a vertical velocity gradient that improves the angle coverage of steeply dipping reflectors.

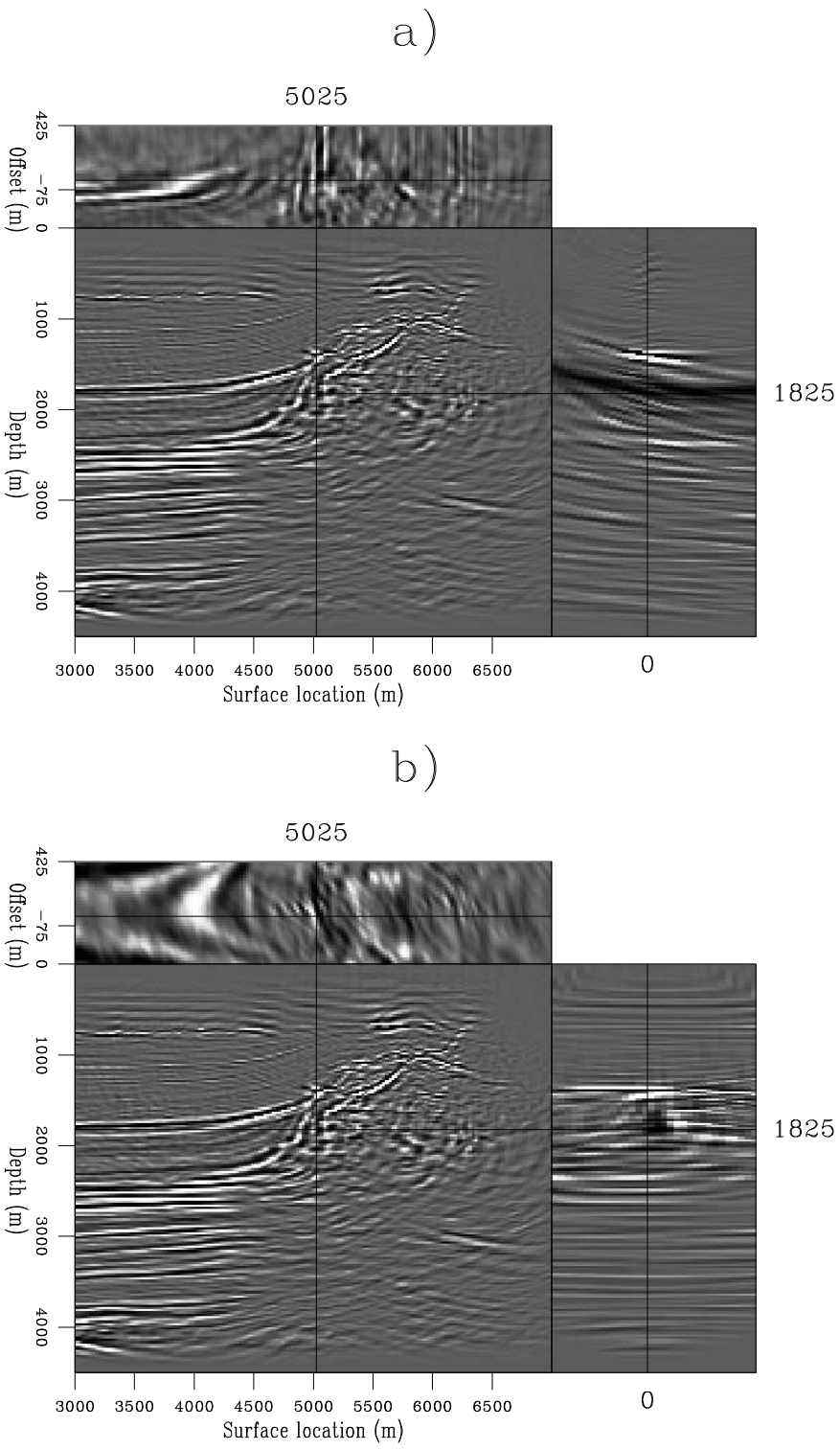

Figure 6: Migrated images of North Sea data set. Orthogonal sections cut through offset-domain CIG cubes: a) HOCIG cube, b) VOCIG cube. Notice the artifacts in both cubes. biondo1-Cube-both-v7newsc-overn [CR]

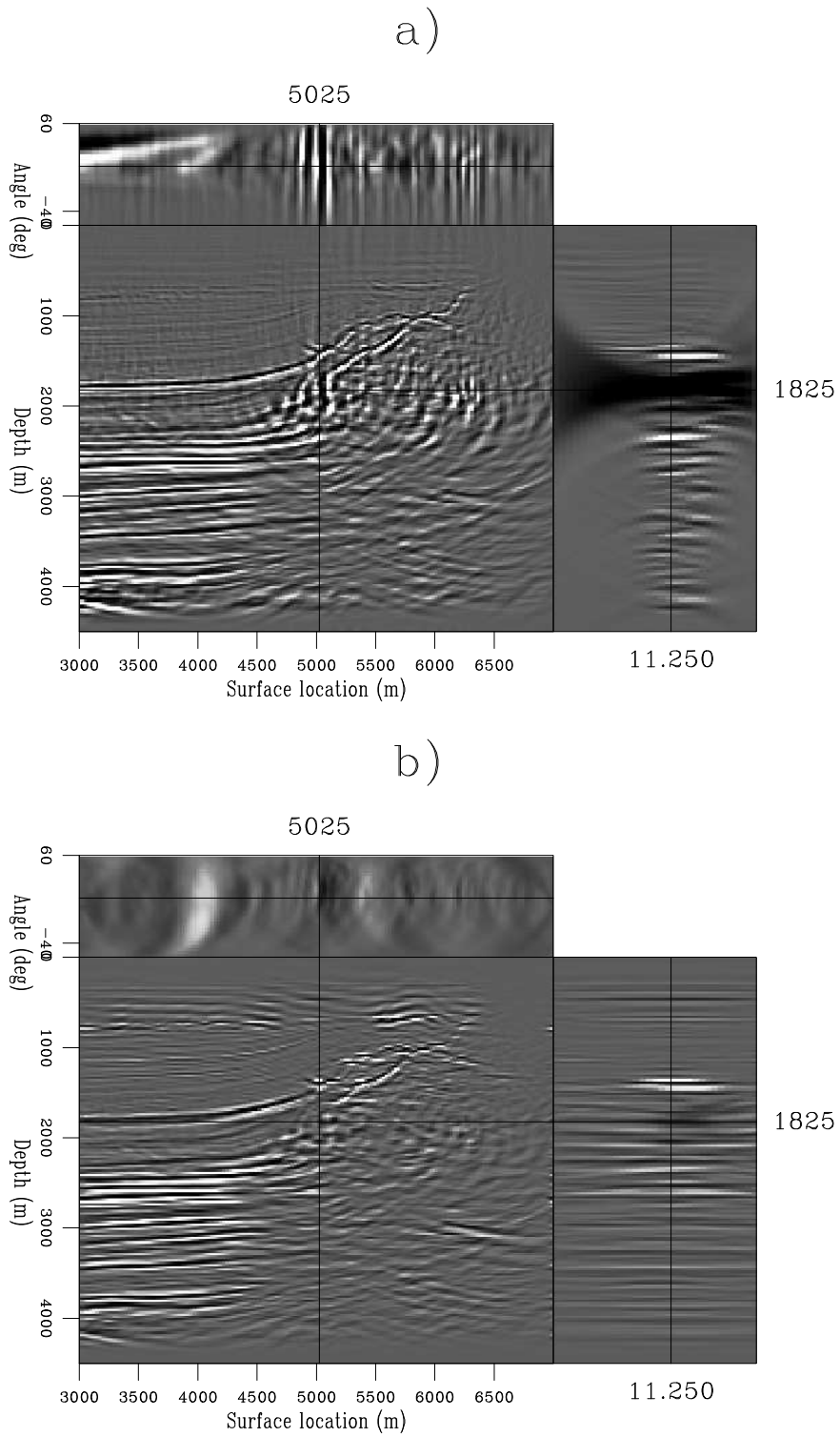

Figure 7: Orthogonal sections cut through ADCIG cubes: a) ADCIG computed from HOCIG cube, b) ADCIG computed from VOCIG cube. Notice the artifacts in both cubes that are related to the artifacts visible in the corresponding offset-domain CIG cubes (Figure 6). biondo1-Ang-Cube-both-v7newsc-overn [CR]

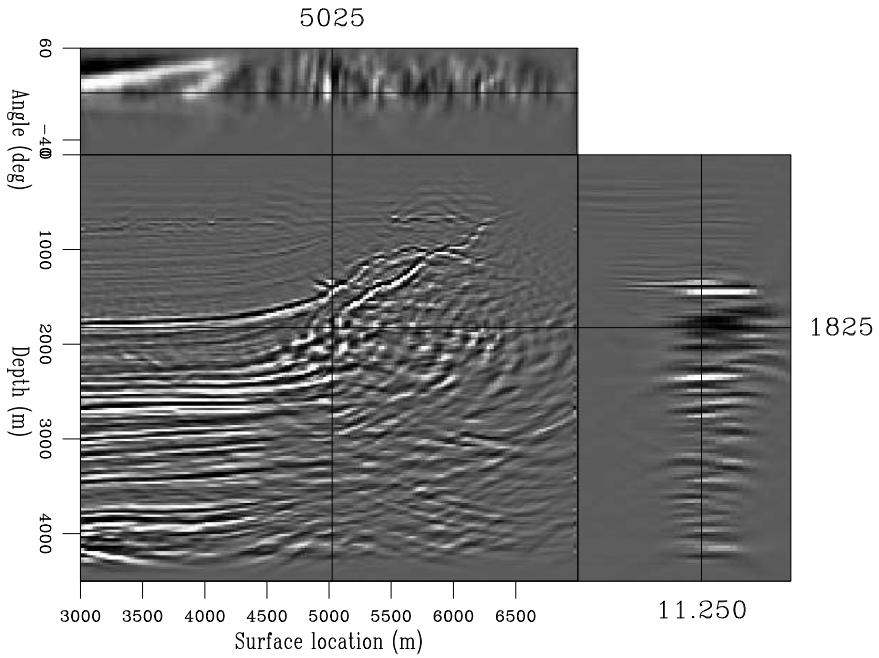

Figure 8: Orthogonal sections cut through the ADCIG cube that was obtained by merging the cubes displayed in Figure 7 using the proposed method. Notice the lack of artifacts compared with Figure 7. biondo1-Ang-Cube-merge-v7newsc [CR]

Transformation of HOCIGs and VOCIGs to GOCIGs

Figure 12 illustrates the differences between HOCIGs and VOCIGs caused by the image-point shift, and it demonstrates that the image-point shift is corrected by the transformation to GOCIGs described in equations (9) and (10).

Figures 12a and 12b show orthogonal sections cut through the offset-domain image cubes in the case of the low velocity migration. Figure 12a displays the horizontal-offset image cube, while Figure 12b displays the vertical-offset image cube. Notice that the offset axis in Figure 12b has been reversed to facilitate its visual correlation with the image cube displayed in Figure 12a. The side faces of the cubes display the CIGs taken at the surface location corresponding to the apparent geological dip of 45 degrees. The events in the two types of CIGs have similar shapes, as expected from the geometric analysis presented in a previous section ($\cos\alpha = \sin\alpha$ when α= 45 degrees), but their extents are different. The differences between the two image cubes are more apparent when comparing the front faces, which show the image at a constant offset of 110 meters (-110 meters in Figure 12b). These differences are due to the differences in image-point shift for the two offset directions [equation (11) and equation (12)].

Figure 12c and 12d show the image cubes of Figures 12a and 12b after the application of the transformations to GOCIG, described in equations (9) and (10), respectively. The two transformed cubes are almost identical, because both the offset stretching and the image-point shift have been removed. The only significant differences are visible in the front face for the reflections corresponding to the top of the sphere. These reflections cannot be fully cap-

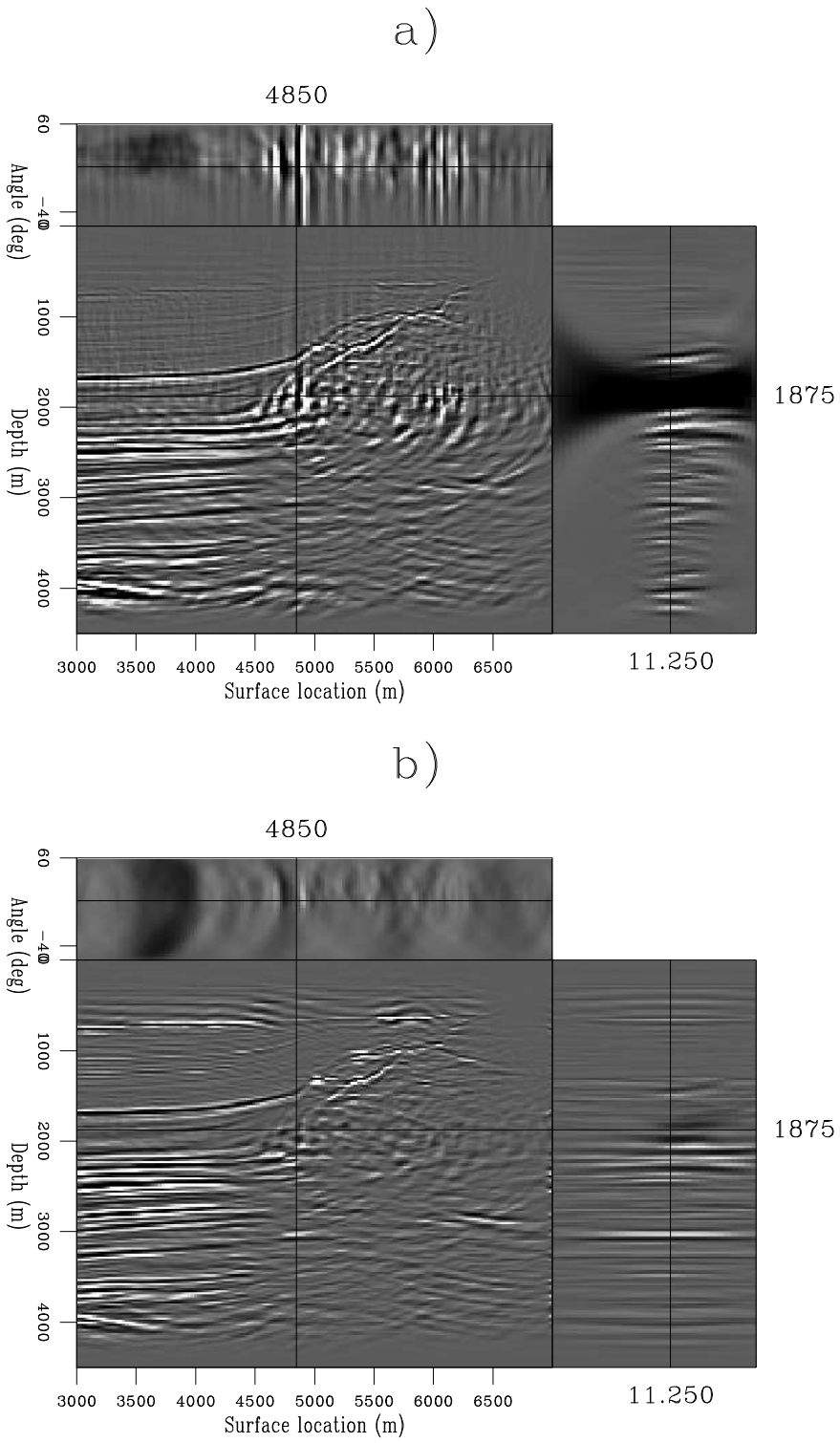

Figure 9: Migrated images of North Sea data set. The migration slowness had been scaled by 1.04 with respect to the migration slowness used for the images shown in Figures 6–8. Orthogonal sections cut through ADCIG cubes: a) ADCIG computed from HOCIG cube, b) ADCIG computed from VOCIG cube. Notice that the artifacts obscure the moveout information in both cubes. biondo1-Ang-Cube-both-v7new-overn [CR]

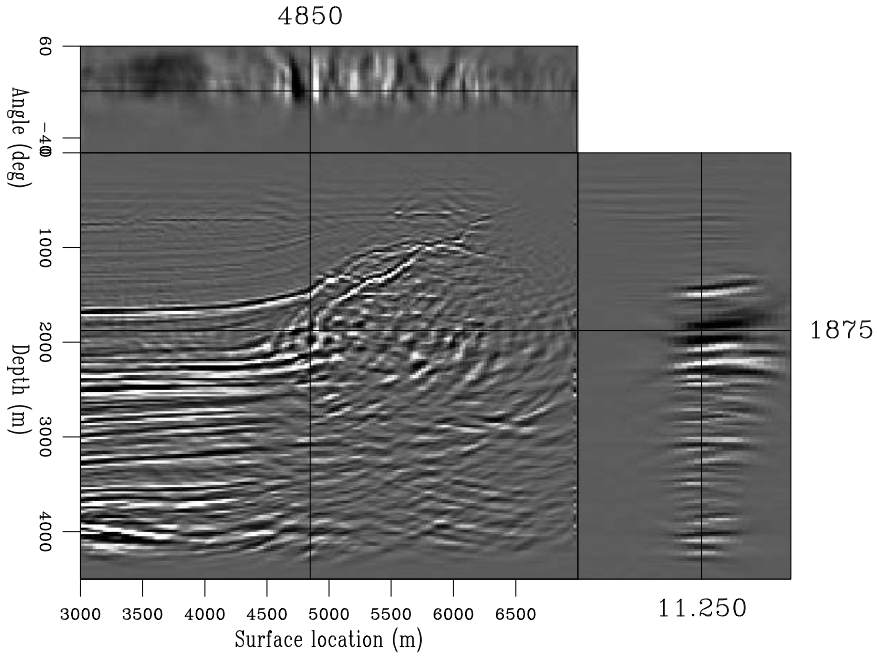

Figure 10: Orthogonal sections cut through the ADCIG cube that was obtained by merging the cubes displayed in Figure 9 using the proposed method. Notice the typical upward smile in the moveouts from both the salt edge and the flattish event above it. biondo1-Ang-Cube-merge-v7new [CR]

tured within the vertical-offset image cube because the expression in equation (10) diverges as α goes to zero. Similarly, reflections from steeply dipping events are missing from the horizontal-offset image cube because the expression in equation (9) diverges as α goes to 90 degrees.

Image mispositioning in ADCIGs migrated with wrong velocity

In a previous section, we demonstrated that in an ADCIG cube the imaging point I_γ lies on the line normal to the apparent geological dip and passing through the point where the source and receiver rays cross (Figure 3). This geometric property enabled us to define the analytical relationship between reflector movement and traveltime perturbation expressed in equation (15). This important result is verified by the numerical experiment shown in Figure 13. This figure compares the images of the spherical reflector obtained using the low velocity (slowness scaled by $\rho = 1.04$) with the reflector position computed analytically under the assumption that I_γ is indeed the image point in an ADCIG. Because both the true and the migration velocity functions are constant, the migrated reflector location can be computed exactly by a simple "kinematic migration" of the recorded events. This process takes into account the difference in propagation directions between the "true" events and the "migrated" events caused by the scaling of the velocity function. Appendix C derives the equations used to compute the migrated reflector location as a function of ρ, α_ρ, and γ_ρ.

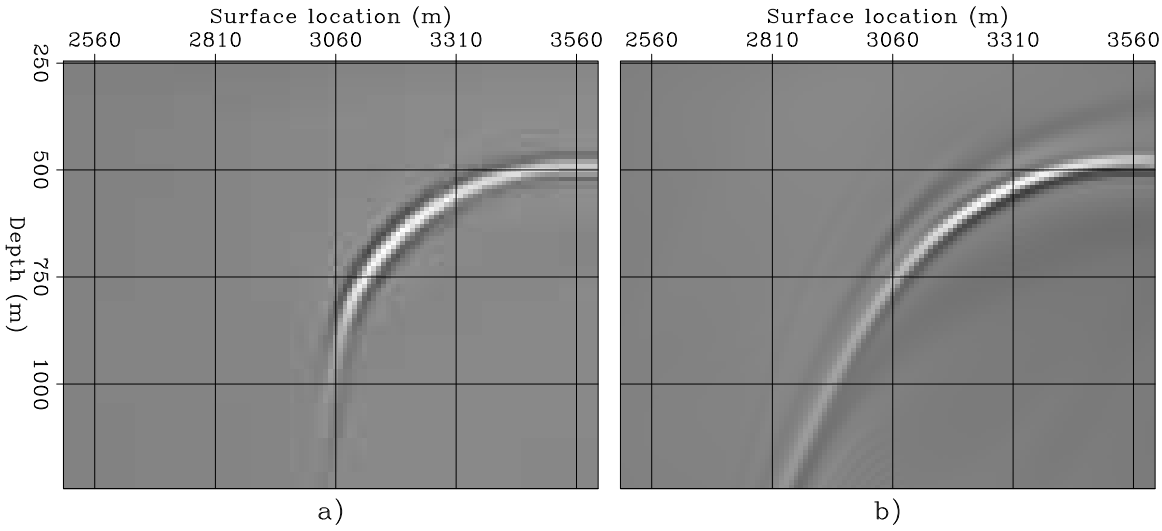

Figure 11: Images of the synthetic data set obtained with a) correct velocity, b) too low velocity ($\rho = 1.04$). biondo1-Mig-zo-overn [CR]

The images shown in the six panels in Figure 13 correspond to six different apparent aperture angles: a) $\gamma_\rho = 0$, b) $\gamma_\rho = 10$, c) $\gamma_\rho = 20$, d) $\gamma_\rho = 30$, e) $\gamma_\rho = 40$, f) $\gamma_\rho = 50$. The black lines superimposed onto the images are the corresponding reflector locations predicted by the relationships derived in Appendix C. The analytical lines perfectly track the migrated images for all values of γ_ρ. The lines terminate when the corresponding event was not recorded by the data acquisition geometry (described above). The images extend beyond the termination of the analytical lines because the truncation artifacts are affected by the finite-frequency nature of the seismic signal, and thus they are not predicted by the simple kinematic modeling described in Appendix C.

RESIDUAL MOVEOUT IN ADCIGS

The inconsistencies between the migrated images at different aperture angles are the primary source of information for velocity updating during Migration Velocity Analysis (MVA). Figure 13 demonstrated how the reflector mispositioning caused by velocity errors can be exactly predicted by a kinematic migration that assumes the image point to lie on the normal to the apparent geological dip. However, this exact prediction is based on the knowledge of the true velocity model. Of course, this condition is not realistic when we are actually trying to estimate the true velocity model by MVA. In these cases, we first measure the inconsistencies between the migrated images at different aperture angles, and then we "invert" these measures into perturbations of the velocity model.

An effective and robust method for measuring inconsistencies between images is to compute semblance scans as a function of one "residual moveout" (RMO) parameter, and then pick the maxima of the semblance scan. This procedure is most effective when the residual move-

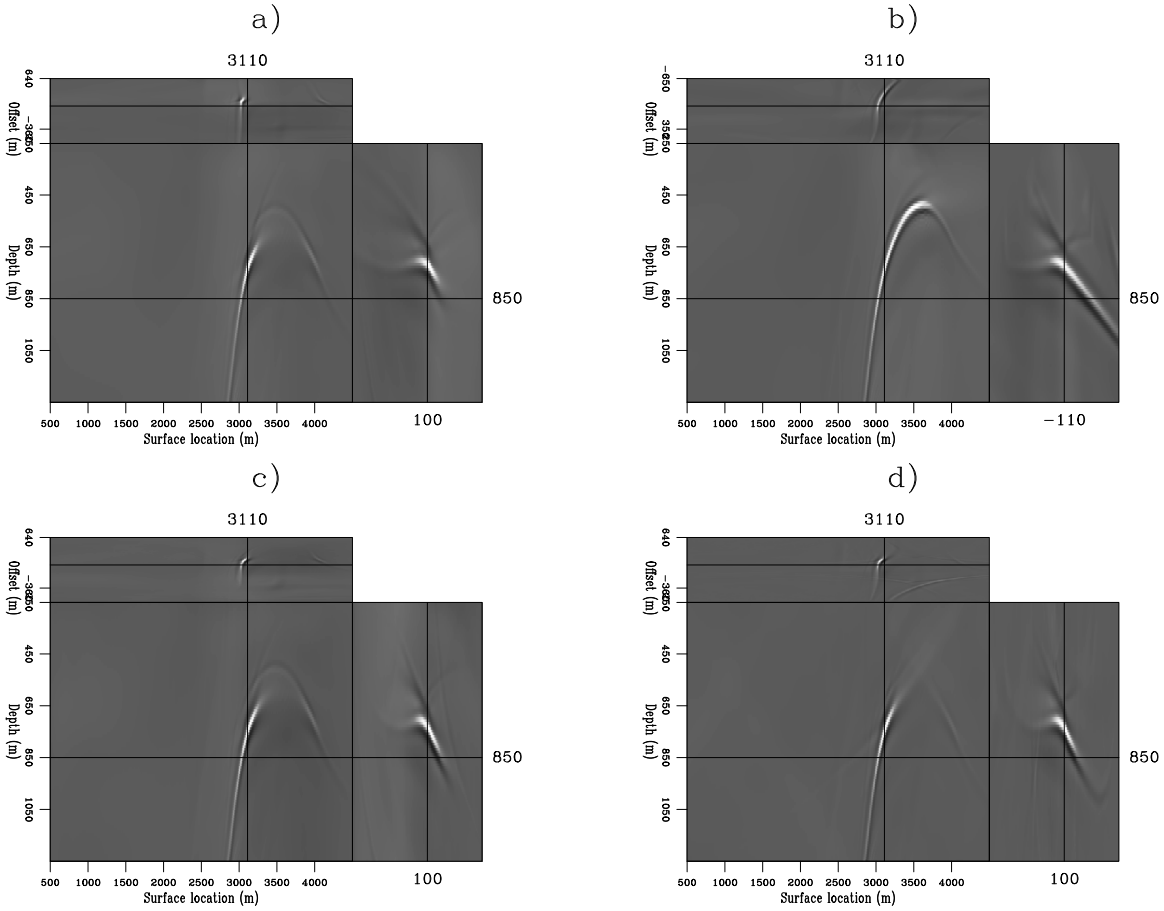

Figure 12: Orthogonal sections cut through offset-domain CIG cubes obtained with too low velocity ($\rho = 1.04$): a) HOCIG cube, b) VOCIG cube, c) GOCIG cube computed from HOCIG cube, d) GOCIG cube computed from VOCIG cube. Notice the differences between the HOCIG (panel a) and the VOCIG (panel b) cubes, and the similarities between the GOCIG cubes (panel c and panel d). biondo1-Cube-slow-4p-overn [CR]

out function used for computing the semblance scans closely approximates the true moveouts in the images. In this section, we use the kinematic properties that we derived and illustrated in the previous sections to derive two alternative RMO functions for scanning ADCIGs computed from wavefield-continuation migration.

As discussed above, the exact relationships derived in Appendix C cannot be used, because the true velocity function is not known. Thus we cannot realistically estimate the changes in ray-propagation directions caused by velocity perturbations. However, we can linearize the relations and estimate the reflector movement by assuming that the raypaths are stationary. This assumption is consistent with the typical use of measured RMO functions by MVA procedures. For example, in a tomographic MVA procedure the velocity is updated by applying a tomographic scheme that "backprojects" the image inconsistencies along unperturbed raypaths. Furthermore, the consequences of the errors introduced by neglecting ray bending are

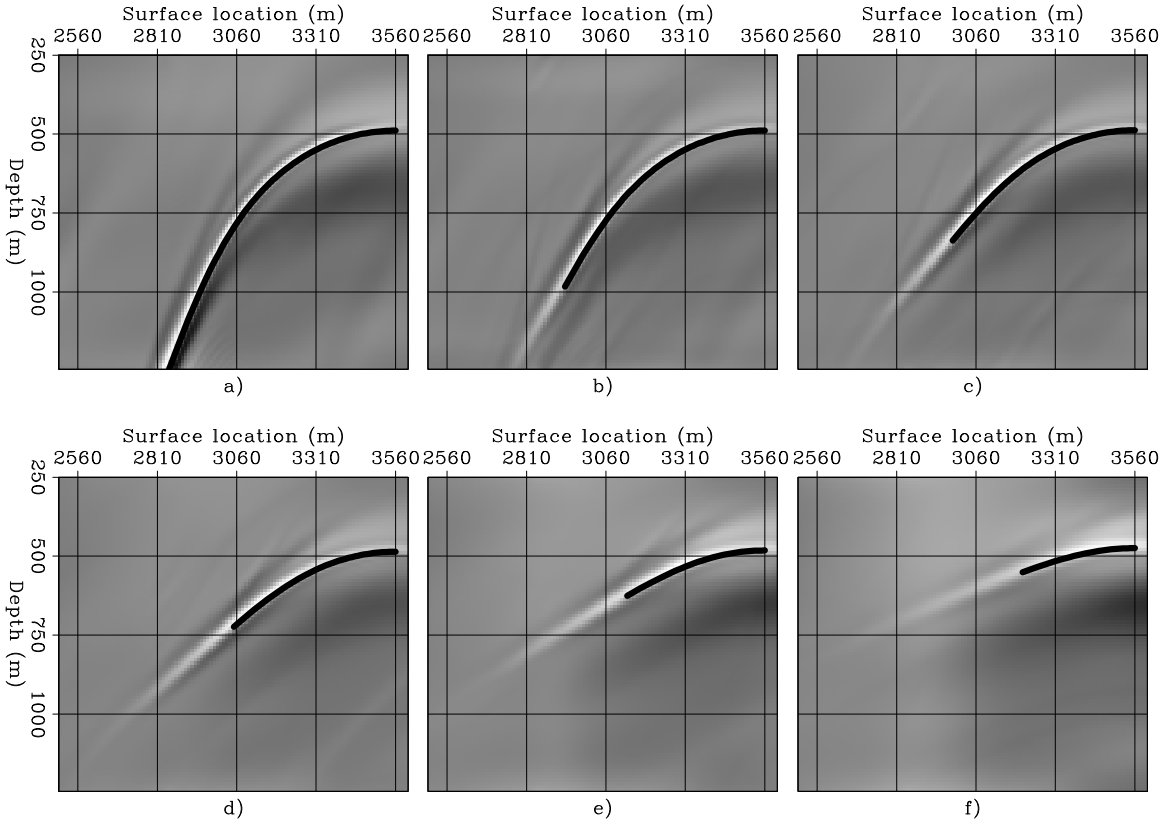

Figure 13: Comparison of the actual images obtained using the low velocity, with the reflector position computed analytically under the assumption that the image point lies on the normal to the apparent geological dip (I_γ in Figure 3). The black lines superimposed onto the images are the reflector locations predicted by the relationships presented in Appendix C. The six panels correspond to six different apparent aperture angles: a) $\gamma_\rho = 0$ b) $\gamma_\rho = 10$ c) $\gamma_\rho = 20$ d) $\gamma_\rho = 30$ e) $\gamma_\rho = 40$ f) $\gamma_\rho = 50$. biondo1-Tomo-slow-4p-overn [CR]

significantly reduced by the fact that RMO functions describe the movements of the reflectors relative to the reflector position imaged at normal incidence ($\gamma = 0$), not the absolute movements of the reflectors with respect to the true (unknown) reflector position.

Appendix D derives two expressions for the RMO shift along the normal to the reflector ($\Delta\mathbf{n}_{\text{RMO}}$), under the assumptions of stationary raypaths and constant scaling of the slowness function by a factor ρ. The first expression is [equation (D-7)]:

$$\Delta\mathbf{n}_{\text{RMO}} = \frac{1-\rho}{1-\rho\,(1-\cos\alpha)}\,\frac{\sin^2\gamma}{\left(\cos^2\alpha-\sin^2\gamma\right)}z_0\,\mathbf{n}, \tag{21}$$

where z_0 is the depth at normal incidence.

The second RMO function is directly derived from the first by assuming flat reflectors ($\alpha = 0$) [equation (D-8)]:

$$\Delta\mathbf{n}_{\text{RMO}} = (1-\rho)\tan^2\gamma\, z_0\,\mathbf{n}. \tag{22}$$

As expected, in both expressions the RMO shift is null at normal incidence ($\gamma = 0$), and when the migration slowness is equal to the true slowness ($\rho = 1$).

According to the first expression [equation (21)], the RMO shift increases as a function of the apparent geological dip $|\alpha|$. The intuitive explanation for this behavior is that the rays become longer as the apparent geological dip increases, and consequently the effects of the slowness scaling increase. The first expression is more accurate than the second one when the spatial extent of the velocity perturbations is large compared to the raypath length, and consequently the velocity perturbations are uniformly felt along the entire raypaths. Its use might be advantageous at the beginning of the MVA process when slowness errors are typically large scale. However, it has the disadvantage of depending on the reflector dip α, and thus its application is somewhat more complex.

The second expression is simpler and is not as dependent on the assumption of large-scale velocity perturbations as the first one. Its use might be advantageous for estimating small-scale velocity anomalies at a later stage of the MVA process, when the gross features of the slowness function have been already determined.

To test the accuracy of the two RMO functions we will use the migration results of a synthetic data set acquired over a spherical reflector. This data set was described in the previous section. Figure 14 illustrates the accuracy of the two RMO functions when predicting the actual RMO in the migrated images obtained with a constant slowness function with $\rho = 1.04$. The four panels show the ADCIGs corresponding to different apparent reflector dip: a) α = 0; b) α = 30; c) α = 45; d) α = 60. Notice that the vertical axes change across the panels; in each panel the vertical axis is oriented along the direction normal to the respective apparent geological dip. The solid lines superimposed onto the images are computed using equation (21), whereas the dashed lines are computed using equation (22). As in Figure 13, the images extend beyond the termination of the analytical lines because of the finite-frequency nature of the truncation artifacts.

The migrated images displayed in Figure 14 were computed by setting both the true and the migration slowness function to be constant. Therefore, this case favors the first RMO function [equation (21)] because it nearly meets the conditions under which equation (21) was derived in Appendix D. Consequently, the solid lines overlap the migration results for all dip angles. This figure demonstrates that, when the slowness perturbation is sufficiently small (4 % in this case), the assumption of stationary raypaths causes only small errors in the predicted RMO.

On the contrary, the dashed lines predicted by the second RMO function [equation (22)] are an acceptable approximation of the actual RMO function only for small dip angles (up to 30 degrees). For large dip angles, a value of ρ substantially higher than the correct one would be necessary to fit the actual RMO function with equation (22). If this effect of the reflector dip is not properly taken into account, the false indications provided by the inappropriate use of equation (22) can prevent the MVA process from converging.

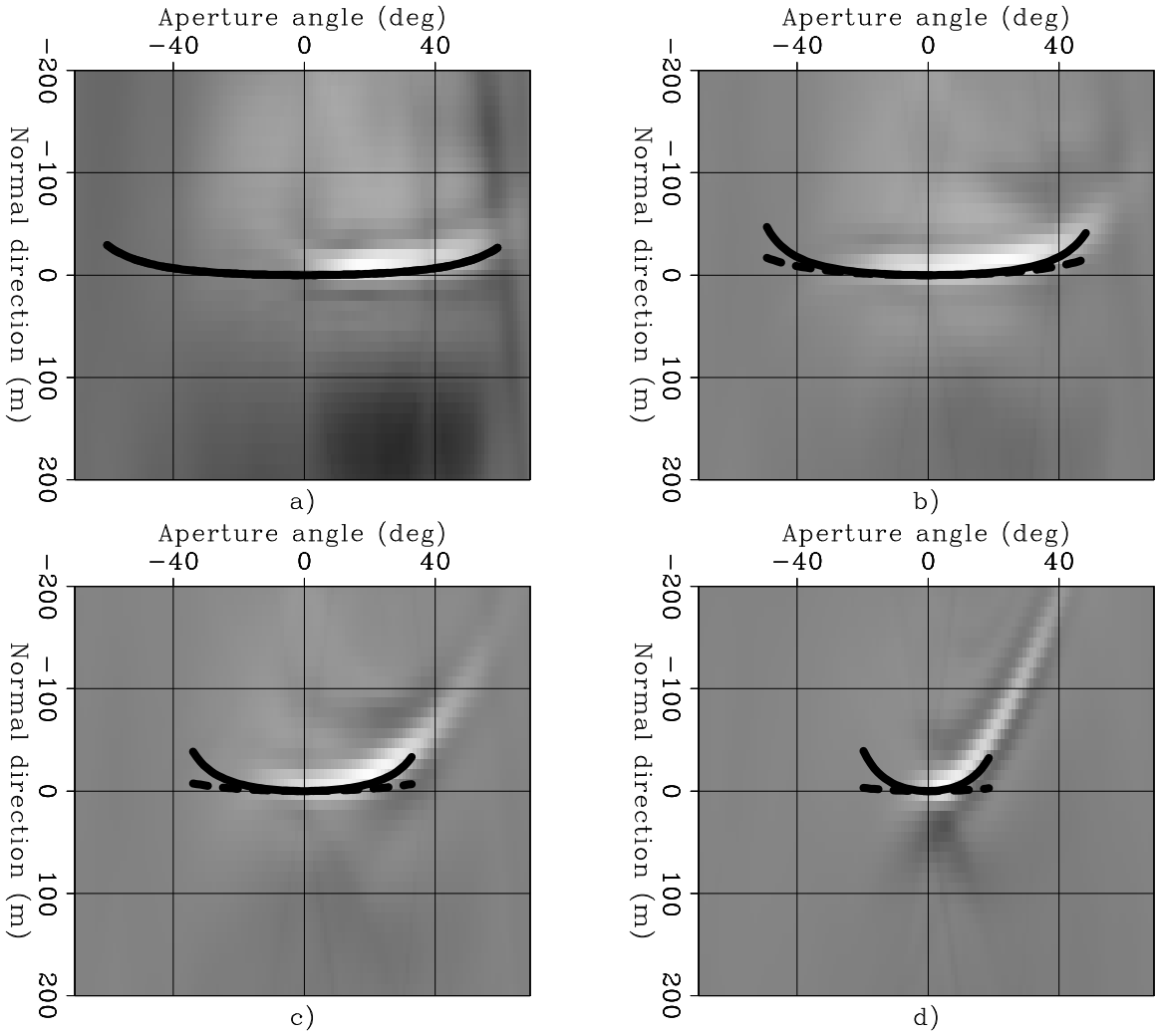

Figure 14: ADCIGs for four different apparent reflector dips: a) α = 0; b) α = 30; c) α = 45; d) α = 60 with $\rho = 1.04$. Superimposed onto the images are the RMO functions computed using equation (21) (solid lines), and using equation (22) (dashed lines). Notice that the vertical axes change across the panels; in each panel the vertical axis is oriented along the direction normal to the respective apparent geological dip. biondo1-Ang-Cig-slow-4p-overn [CR]

CONCLUSIONS

We analyzed the kinematic properties of ADCIGs in presence of velocity errors. We proved that in the angle domain the image point lies along the normal to the apparent reflector dip. This geometric property of ADCIGs makes them immune to the image-point dispersal and thus attractive for MVA.

We derived a quantitative relationship between image-point movements and traveltime perturbations caused by velocity errors, and verified its validity with a synthetic-data example. This relationship should be at the basis of velocity-updating methods that exploit the velocity information contained in ADCIGs.

Our analysis leads to the definition of two RMO functions that can be used to measure inconsistencies between migrated images at different aperture angles. The RMO functions describe the relative movements of the imaged reflectors only approximately, because they are derived assuming stationary raypaths. However, a synthetic example shows that, when the velocity perturbation is sufficiently small, one of the proposed RMO functions is accurate for a wide range of reflector dips and aperture angles.

The insights gained from our kinematic analysis explain the strong artifacts that affect conventional ADCIG in presence of steeply dipping reflectors. They also suggest a procedure for overcoming the problem: the computation of vertical-offset CIGs (VOCIGs) followed by the combination of VOCIGs with conventional HOCIGs. We propose a simple and robust scheme for combining HOCIGs and VOCIGs. A North Sea data example clearly illustrates both the need for and the advantages of our method for computing ADCIGs in presence of a vertical salt edge.

ACKNOWLEDGMENTS

We thank Guojian Shan for helping in the development of the program that we used to migrate both the synthetic and the real data sets. We also thank Henri Calandra and TotalFinaElf for making the North Sea data set available to the Stanford Exploration Project (SEP).

REFERENCES

Baysal, E., Kosloff, D. D., and Sherwood, J. W. C., 1983, Reverse time migration: Geophysics, **48**, no. 11, 1514–1524.

Biondi, B., and Sava, P., 1999, Wave-equation migration velocity analysis: 69th Ann. Internat. Meeting, Soc. of Expl. Geophys., Expanded Abstracts, 1723–1726.

Biondi, B., and Shan, G., 2002, Prestack imaging of overturned reflections by reverse time migration: 72nd Ann. Internat. Meeting, Soc. of Expl. Geophys., Expanded Abstracts, 1284–1287.

Biondi, B., 2003, Equivalence of source-receiver migration and shot-profile migration: Geophysics, accepted for publication.

Clapp, R., and Biondi, B., 2000, Tau domain migration velocity analysis using angle CRP gathers and geologic constraints: 70th Ann. Internat. Mtg., Soc. Expl. Geophys., 926–929.

de Bruin, C. G. M., Wapenaar, C. P. A., and Berkhout, A. J., 1990, Angle-dependent reflectivity by means of prestack migration: Geophysics, **55**, no. 9, 1223–1234.

de Hoop, M., Le Rousseau, J., and Biondi, B., 2002, Symplectic structure of wave-equation imaging: A path-integral approach based on the double-square-root equation: Journal of Geophysical Research, accepted for publication.

Etgen, J., 1986, Prestack reverse time migration of shot profiles: SEP–**50**, 151–170, `http://sep.stanford.edu/research/reports`.

Etgen, J., 1990, Residual prestack migration and interval velocity estimation: Ph.D. thesis, Stanford University.

Liu, W., Popovici, A., Bevc, D., and Biondi, B., 2001, 3-D migration velocity analysis for common image gathers in the reflection angle domain: 69th Ann. Internat. Meeting, Soc. of Expl. Geophys., Expanded Abstracts, 885–888.

Mosher, C. C., Foster, D. J., and Hassanzadeh, S., 1997, Common angle imaging with offset plane waves: 67th Annual Internat. Mtg., Soc. Expl. Geophys., Expanded Abstracts, 1379–1382.

Mosher, C., Jin, S., and Foster, D., 2001, Migration velocity analysis using common angle image gathers: 71st Ann. Internat. Mtg., Soc. of Expl. Geophys., 889–892.

Prucha, M., Biondi, B., and Symes, W., 1999, Angle-domain common-image gathers by wave-equation migration: 69th Ann. Internat. Meeting, Soc. Expl. Geophys., Expanded Abstracts, 824–827.

Rickett, J., and Sava, P., 2002, Offset and angle-domain common image-point gathers for shot-profile migration: Geophysics, **67**, 883–889.

Sava, P., and Fomel, S., 2002, Angle-domain common-image gathers by wavefield continuation methods: Geophysics, accepted for publication.

Sava, P., Biondi, B., and Fomel, S., 2001, Amplitude-preserved common image gathers by wave-equation migration: 71st Ann. Internat. Meeting, Soc. Expl. Geophys., Expanded Abstracts, 296–299.

Schultz, P. S., and Claerbout, J. F., 1978, Velocity estimation and downward-continuation by wavefront synthesis: Geophysics, **43**, no. 4, 691–714.

Stork, C., Kitchenside, P., Yingst, D., Albertin, U., Kostov, C., Wilson, B., Watts, D., Kapoor, J., and Brown, G., 2002, Comparison between angle and offset gathers from wave equation migration and Kirchhoff migration: 72nd Ann. Internat. Meeting, Soc. of Expl. Geophys., Expanded Abstracts, 1200–1203.

Wapenaar, K., Van Wijngaarden, A., van Geloven, W., and van der Leij, T., 1999, Apparent AVA effects of fine layering: Geophysics, **64**, no. 6, 1939–1948.

Whitmore, N. D., 1983, Iterative depth migration by backward time propagation: 53rd Annual Internat. Mtg., Soc. Expl. Geophys., Expanded Abstracts, Session:S10.1.

Xie, X. B., and Wu, R. S., 2002, Extracting angle domain information from migrated wavefield: 72nd Ann. Internat. Mtg., Soc. Expl. Geophys., 1360–1363.

APPENDIX A

PROOF THAT THE TRANSFORMATION TO GOCIG CORRECTS FOR THE IMAGE-POINT SHIFT

This appendix proves that by applying the offset transformations described in equations (9) and (10) we automatically remove the image-point shift characterized by equations (11) and (12). The demonstration for the VOCIG transformation is similar to the one for the HOCIG transformation, and thus we present only the demonstration for the HOCIGs. HOCIGs are transformed into GOCIGs by applying the following change of variables of the offset axis x_h, in the vertical wavenumber k_z and horizontal wavenumber k_x domain:

$$x_h = \frac{\widetilde{h}_0}{\cos\alpha} = \text{sign}(\tan\alpha)\widetilde{h}_0\sqrt{1+\tan^2\alpha} = \text{sign}\left(\frac{k_x}{k_z}\right)\widetilde{h}_0\left(1+\frac{k_x^2}{k_z^2}\right)^{\frac{1}{2}}. \tag{A-1}$$

For the sake of simplicity, in the rest of the appendix we will drop the sign in front of expression (A-1) and consider only the positive values of k_x/k_z.

We want to prove that by applying (A-1) we also automatically shift the image by

$$\Delta_z I_{x_h} = -\widetilde{h}_0 \tan\gamma \tan\alpha \sin\alpha \tag{A-2}$$

in the vertical direction, and

$$\Delta_x I_{x_h} = \widetilde{h}_0 \tan\gamma \tan\alpha \cos\alpha \tag{A-3}$$

in the horizontal direction.

The demonstration is carried out in two steps: 1) we compute the kinematics of the impulse response of transformation (A-1) by a stationary-phase approximation of the inverse Fourier transform along k_z and k_x, and 2) we evaluate the dips of the impulse response, relate them to the angles α and γ, and then demonstrate that relations (A-3) and (A-2) are satisfied.

Evaluation of the impulse response of the transformation to GOCIGs

The transformation to GOCIG of an image $I_{x_h}(k_z,k_x,x_h)$ is defined as

$$I_0(k_z,k_x,k_h)=\int d\widetilde{h_0} I_0\left(k_z,k_x,\widetilde{h_0}\right)e^{ik_h\widetilde{h_0}}=\int dx_h\left(\frac{d\widetilde{h_0}}{dx_h}\right)I_{x_h}(k_z,k_x,x_h)e^{ik_hx_h\left(1+\frac{k_x^2}{k_z^2}\right)^{-\frac{1}{2}}}. \tag{A-4}$$

The transformation to GOCIG of an impulse located at $(\bar{z},\bar{x},\bar{x_h})$ is thus (after inverse Fourier transforms):

$$\widetilde{\mathrm{Imp}}\left(z,x,\widetilde{h_0}\right)=\int dk_h\int dx_h\int dk_x\int dk_z\left(\frac{d\widetilde{h_0}}{dx_h}\right)e^{i\left\{k_h\left[\bar{x_h}\left(1+\frac{k_x^2}{k_z^2}\right)^{-\frac{1}{2}}-\widetilde{h_0}\right]+k_z(\bar{z}-z)+k_x(\bar{x}-x)\right\}}. \tag{A-5}$$

We now approximate by stationary phase the inner double integral. The phase of this integral is:

$$\Phi\equiv k_h\left[\bar{x_h}\left(1+\frac{k_x^2}{k_z^2}\right)^{-\frac{1}{2}}-\widetilde{h_0}\right]+k_z(\bar{z}-z)+k_x(\bar{x}-x). \tag{A-6}$$

The stationary path is defined by the solutions of the following system of equations:

$$\frac{\partial\Phi}{\partial k_z} = k_h\bar{x_h}\frac{k_x^2}{k_z^3}\left(1+\frac{k_x^2}{k_z^2}\right)^{-\frac{3}{2}}+(\bar{z}-z)=0, \tag{A-7}$$

$$\frac{\partial\Phi}{\partial k_x} = -k_h\bar{x_h}\frac{k_x}{k_z^2}\left(1+\frac{k_x^2}{k_z^2}\right)^{-\frac{3}{2}}+(\bar{x}-x)=0. \tag{A-8}$$

By moving both $(\bar{z}-z)$ and $(\bar{x}-x)$ to the right of equations (A-7) and (A-8), and then dividing equation (A-7) by equation (A-8), we obtain the following relationship between $(\bar{z}-z)$ and $(\bar{x}-x)$:

$$\frac{\bar{z}-z}{\bar{x}-x}=-\frac{k_x}{k_z}. \tag{A-9}$$

Furthermore, by multiplying equation (A-7) by k_z and equation (A-8) by k_x, and then substituting them appropriately in the phase function (A-6), we can evaluate the phase function along the stationary path as follows:

$$\Phi_{\text{stat}}=k_h\left[\bar{x_h}\left(1+\frac{k_x^2}{k_z^2}\right)^{-\frac{1}{2}}-\widetilde{h_0}\right], \tag{A-10}$$

which becomes, by substituting equation (A-9),

$$\Phi_{\text{stat}}=k_h\left\{-\bar{x_h}\left[1+\frac{(\bar{z}-z)^2}{(\bar{x}-x)^2}\right]^{-\frac{1}{2}}-\widetilde{h_0}\right\}. \tag{A-11}$$

Notice that the minus sign comes from the sign function in expression (A-1). By substituting expression (A-11) in equation (A-5) it is immediate to evaluate the kinematics of the impulse response as follows:

$$\widetilde{h_0} = -x_h \left[1 + \frac{(\bar{z}-z)^2}{(\bar{x}-x)^2} \right]^{-\frac{1}{2}}. \tag{A-12}$$

Evaluation of the image shift as a function of α and γ

The final step is to take the derivative of the impulse response of equation (A-12) and use the relationships of these derivatives with $\tan\alpha$ and $\tan\gamma$:

$$\frac{\partial z}{\partial x} = \tan\alpha = \sqrt{\frac{x_h^2}{\widetilde{h_0}^2} - 1}, \tag{A-13}$$

$$-\frac{\partial z}{\partial x_h} = \tan\gamma = -(\bar{x}-x)\frac{\frac{x_h}{\widetilde{h_0}}}{\sqrt{\frac{x_h^2}{\widetilde{h_0}^2}-1}} = -(\bar{z}-z)\frac{\frac{x_h}{\widetilde{h_0}}}{\frac{x_h^2}{\widetilde{h_0}^2}-1}. \tag{A-14}$$

Substituting equations (A-13) and (A-14) into the following relationships:

$$\Delta_z I_{x_h} = \bar{z}-z = -\widetilde{h_0}\tan\gamma\tan\alpha\sin\alpha, \tag{A-15}$$

$$\Delta_x I_{x_h} = \bar{x}-x = \widetilde{h_0}\tan\gamma\tan\alpha\cos\alpha, \tag{A-16}$$

and after some algebraic manipulation, we prove the thesis.

APPENDIX B

This appendix demonstrates equations (19) in the main text: that for energy dipping at an angle α in the (z,x) plane, the wavenumber k_n along the normal to the dip is linked to the wavenumbers k_z and k_x by the following relationships:

$$k_n = \frac{k_z}{\cos\alpha} = \frac{k_x}{\sin\alpha}. \tag{B-1}$$

For energy dipping at an angle α the wavenumbers satisfy the well-known relationship

$$\tan\alpha = \frac{k_x}{k_z}, \tag{B-2}$$

where the positive sign is determined by by the conventions defined in Figure 1. The wavenumber k_n is related to k_x and k_z by the axes rotation

$$k_n = k_z\cos\alpha + k_x\sin\alpha. \tag{B-3}$$

Substituting equation (B-2) into equation (B-3) we obtain

$$k_n = \frac{k_z}{\cos\alpha}\left(\cos^2\alpha + \tan\alpha\cos\alpha\sin\alpha\right) = \frac{k_z}{\cos\alpha}\left(\cos^2\alpha + \sin^2\alpha\right) = \frac{k_z}{\cos\alpha}, \tag{B-4}$$

or,

$$k_n = \frac{k_x}{\sin\alpha}\left(\cot\alpha\sin\alpha\cos\alpha + \sin^2\alpha\right) = \frac{k_x}{\sin\alpha}\left(\cos^2\alpha + \sin^2\alpha\right) = \frac{k_x}{\sin\alpha}. \tag{B-5}$$

APPENDIX C

In this appendix we derive the equations for the "kinematic migration" of the reflections from a sphere, as a function of the ratio ρ between the true constant slowness S and the migration slowness $S_\rho = \rho S$. For a given ρ we want to find the coordinates of the imaging point $I_\gamma(z_\gamma, x_\gamma)$ as a function of the apparent geological dip α_ρ and the apparent aperture angle γ_ρ. Central to our derivation is the assumption that the imaging point I_γ lies on the normal to the apparent reflector dip passing through $\bar{I}$, as represented in Figure 3.

The first step is to establish the relationships between the true α and γ and the apparent α_ρ and γ_ρ. This can be done through the relationships between the propagation directions of the source/receiver rays (respectively marked as the angles β and δ in Figure 1), and the event time dips, which are independent on the migration slowness. The true β and δ can be thus estimated as follows:

$$\beta = \arcsin\left(\rho\sin\beta_\rho\right) = \arcsin\left[\rho\sin\left(\alpha_\rho - \gamma_\rho\right)\right], \tag{C-1}$$

$$\delta = \arcsin\left(\rho\sin\delta_\rho\right) = \arcsin\left[\rho\sin\left(\alpha_\rho + \gamma_\rho\right)\right]; \tag{C-2}$$

and then the true α and γ are:

$$\alpha = \frac{\beta+\delta}{2}, \quad \text{and} \quad \gamma = \frac{\delta-\beta}{2}. \tag{C-3}$$

Next step is to take advantage of the fact that the reflector is a sphere, an thus that the coordinates $(\hat{z}, \hat{x})$ of the true reflection point are uniquely identified by the dip angle α as follows:

$$\hat{z} = (z_c - R\cos\alpha), \quad \text{and} \quad \hat{x} = (x_c + R\sin\alpha), \tag{C-4}$$

where (z_c, x_c) are the coordinates of the center of the sphere and R is its radius.

The midpoint, offset, and traveltime of the event can be found by applying simple trigonometry (see Sava and Fomel (2002)) as follows:

$$x_{h\,\text{surf}} = \frac{\sin\gamma\cos\gamma}{\cos^2\alpha - \sin^2\gamma}\hat{z}, \tag{C-5}$$

$$x_{m\,\text{surf}} = \hat{x} + \frac{\sin\alpha\cos\alpha}{\cos^2\alpha - \sin^2\gamma}\hat{z}, \tag{C-6}$$

$$t_D = 2S\frac{\cos\alpha\cos\gamma}{\cos^2\alpha - \sin^2\gamma}\hat{z}. \tag{C-7}$$

The coordinates of the point $\bar{I}(\bar{z},\bar{x})$, where the source and the receiver rays cross, are:

$$\bar{z} = x_{h\,\text{surf}} \frac{\cos^2\alpha_\rho - \sin^2\gamma_\rho}{\sin\gamma_\rho\cos\gamma_\rho}, \tag{C-8}$$

$$\begin{aligned}\bar{x} &= x_{m\,\text{surf}} - \frac{\sin\alpha_\rho\cos\alpha_\rho}{\cos^2\alpha_\rho - \sin^2\gamma_\rho}\bar{z} = \\ &x_{m\,\text{surf}} - \frac{\sin\alpha_\rho\cos\alpha_\rho}{\cos^2\alpha_\rho - \sin^2\gamma_\rho}\frac{\cos^2\alpha_\rho - \sin^2\gamma_\rho}{\sin\gamma_\rho\cos\gamma_\rho}x_{h\,\text{surf}} = \\ &x_{m\,\text{surf}} - \frac{\sin\alpha_\rho\cos\alpha_\rho}{\sin\gamma_\rho\cos\gamma_\rho}x_{h\,\text{surf}};\end{aligned} \tag{C-9}$$

and the corresponding traveltime $t_{D\rho}$ is:

$$t_{D\rho} = 2\rho S\frac{\cos\alpha_\rho\cos\gamma_\rho}{\cos^2\alpha_\rho - \sin^2\gamma_\rho}\bar{z}. \tag{C-10}$$

Once we have the traveltimes t_D and $t_{D\rho}$, the normal shift $\Delta\mathbf{n}_{\text{tot}}$ can be easily evaluated by applying equation (15) (where the background velocity is S_ρ and the aperture angle is γ_ρ), which yields:

$$\Delta\mathbf{n}_{\text{tot}} = -\frac{\left(t_{D\rho} - t_D\right)}{2\rho S\cos\gamma_\rho}\mathbf{n}. \tag{C-11}$$

We use equation (C-11), together with equations (C-8) and (C-9), to compute the lines superimposed onto the images in Figure 13.

APPENDIX D

In this Appendix we derive the expression for the residual moveout (RMO) function to be applied to ADCIGs computed by wavefield continuation. The derivation follows the derivation presented in Appendix C. The main difference is that in this appendix we assume the rays to be stationary. In other words, we assume that the apparent dip angle α_ρ and aperture angle γ_ρ are the same as the true angles α and γ. This assumption also implies that the (unknown) true reflector position $(\hat{z},\hat{x})$ coincides with the point $\bar{I}(\bar{z},\bar{x})$ where the source and the receiver ray cross.

Given these assumptions, the total traveltime through the perturbed slowness function S_ρ is given by the following expression:

$$t_{D\rho} = 2\rho S\frac{\cos\alpha\cos\gamma}{\cos^2\alpha - \sin^2\gamma}\bar{z}, \tag{D-1}$$

which is different from the corresponding equation in Appendix C [equation (C-10)]. The difference in traveltimes $(t_{D\rho} - t_D)$, where t_D is given by equation equation (C-7), is thus a linear function of the difference in slownesses $[(\rho-1)S]$; that is,

$$t_{D\rho} - t_D = 2\left(\rho - 1\right)S\frac{\cos\alpha\cos\gamma}{\cos^2\alpha - \sin^2\gamma}\bar{z}. \tag{D-2}$$

As in Appendix C, the normal shift $\Delta\mathbf{n}_{\text{tot}}$ can be evaluated by applying equation (15) (where the background velocity is S_ρ and the aperture angle is γ), which yields:

$$\Delta\mathbf{n}_{\text{tot}} = \frac{1-\rho}{\rho}\frac{\cos\alpha}{\cos^2\alpha - \sin^2\gamma}\bar{z}\,\mathbf{n}. \tag{D-3}$$

The RMO function ($\Delta\mathbf{n}_{\text{RMO}}$) describes the relative movement of the image point at any γ with respect to the image point for the normal-incidence event ($\gamma = 0$). From equation (D-3), it follows that the RMO function is:

$$\begin{aligned}\Delta\mathbf{n}_{\text{RMO}} &= \Delta\mathbf{n}_{\text{tot}}(\gamma) - \Delta\mathbf{n}_{\text{tot}}(\gamma=0) = \\ &\frac{1-\rho}{\rho}\left[\frac{\cos\alpha}{\cos^2\alpha - \sin^2\gamma} - \frac{1}{\cos\alpha}\right]\bar{z}\,\mathbf{n} = \\ &\frac{1-\rho}{\rho}\frac{\sin^2\gamma}{\left(\cos^2\alpha - \sin^2\gamma\right)\cos\alpha}\bar{z}\,\mathbf{n}.\end{aligned} \tag{D-4}$$

The true depth $\bar{z}$ is not known, but at normal incidence it can be estimated as a function of the migrated depth z_0 by inverting the following relationship:

$$z_0 = \left(\frac{1-\rho}{\rho\cos\alpha} + 1\right)\bar{z}, \tag{D-5}$$

as:

$$\bar{z} = \left[\frac{\rho\cos\alpha}{1-\rho\,(1-\cos\alpha)}\right]z_0. \tag{D-6}$$

Substituting relation (D-6) in equation (D-4) we obtain the result:

$$\Delta\mathbf{n}_{\text{RMO}} = \frac{1-\rho}{1-\rho\,(1-\cos\alpha)}\frac{\sin^2\gamma}{\left(\cos^2\alpha - \sin^2\gamma\right)}z_0\,\mathbf{n}, \tag{D-7}$$

which for flat reflectors ($\alpha = 0$) simplifies into:

$$\Delta\mathbf{n}_{\text{RMO}} = (1-\rho)\tan^2\gamma\; z_0\,\mathbf{n}. \tag{D-8}$$

In Figure 14, the solid lines superimposed into the images are computed using equation (D-7), whereas the dashed lines are computed using equation (D-8).